



# A new discrimination scheme for oceanic ferromanganese deposits using high field strength and rare earth elements



P. Josso<sup>a,d,\*</sup>, E. Pelleter<sup>a</sup>, O. Pourret<sup>b</sup>, Y. Fouquet<sup>a</sup>, J. Etoubleau<sup>a</sup>, S. Cheron<sup>a</sup>, C. Bollinger<sup>c</sup>

<sup>a</sup> Ifremer, Geochemistry and Metallogeny Laboratory, Plouzané, France

<sup>b</sup> HydriSE, Institut Polytechnique LaSalle Beauvais, 60026 Beauvais cedex, France

<sup>c</sup> Institut Universitaire Européen de la Mer, UMS 3113, Plouzané, France

<sup>d</sup> University of Southampton, National Oceanography Centre, European Way, Southampton SO14 3ZH, UK

## ARTICLE INFO

### Article history:

Received 8 February 2016

Received in revised form 25 August 2016

Accepted 1 September 2016

Available online 12 September 2016

### Keywords:

Ferromanganese mineralization

Hydrogenetic crusts

Nodules

Hydrothermal deposits

Rare earth elements

High field strength elements

Classification

## ABSTRACT

Ferromanganese (Fe–Mn) deposits constitute a ubiquitous mineral type in oceanic settings, with metal (Cu, Ni, Zn, Co, Pt) and rare earth element (REE) enrichments of potential economic interest. Routine analysis of trace elements by ICP–MS has advanced our understanding of the impact of hydrogenetic, diagenetic and hydrothermal processes on the mobility and interaction of high field strength elements (HFSE: Zr and Ti) and REE and yttrium (REY) with Fe–Mn oxyhydroxides. Recent discoveries in the French exclusive economic zone (EEZ) of Wallis and Futuna (southwest Pacific Ocean) have brought new insight into the formation of low temperature (LT) hydrothermal Mn deposits and lead us to reconsider the classification and discrimination diagrams for Fe–Mn deposits and ore-forming processes. Using a suite of LT hydrothermal Fe–Mn crusts from Wallis and Futuna, we investigate how contrasting genetic processes influence the distribution of metals (Mn, Fe, Cu, Ni, and Co), HFSE and REY in hydrogenetic, diagenetic, hydrothermal and mixed-type deposits from different environments in the global ocean. The interaction of the different metal oxide-forming processes indicates that: (i) enrichment of Co, HFSE and REY is favored by hydrogenetic precipitation, (ii) diagenetic processes produce higher Mn, Cu, and Ni concentrations with oxic remobilization in the sedimentary column, while suboxic conditions promote greater Mn and Fe remobilization that competes with the incorporation of Cu and Ni ions in nodules. HFSE and REY derived from seawater are usually low in diagenetic precipitates, which discriminate between hydrogenetic and diagenetic inputs within nodules, (iii) hydrothermal Fe–Mn deposits show strong depletion in HFSE and REY due to rapid formation and high contents of either Fe or Mn oxides. We present a new discrimination scheme for the genetic types of Fe–Mn deposits using a  $10 * (Cu + Ni + Co) - 100 * (Zr + Y + Ce) - (Fe + Mn) / 4$  ternary diagram. The use of HFSE and REY in the classification allows for a more robust discrimination of: (i) each ore-forming process with well-delimited fields, without overlap of metal-rich hydrothermal samples and hydrogenetic samples, (ii) oxic and suboxic diagenesis within nodules, (iii) trends between hydrogenetic and diagenetic end-members forming a continuum, and (iv) mixed genetic types such as the presence of hydrothermal particles within hydrogenetic crust layers. Alternatives are also explored to adapt our discriminative diagram to elements measurable by on-board instruments to aid in exploration at sea.

© 2016 Elsevier B.V. All rights reserved.

## 1. Introduction

Ferromanganese (Fe–Mn) deposits reflect common forms of mineralization in the modern ocean. They may contain significant metal (Cu, Ni, Zn, Co) and rare earth elements plus yttrium (REY) enrichments. Oceanic Fe–Mn deposits include ferromanganese crusts, also referred to as cobalt-rich crusts, polymetallic nodules, and hydrothermal crusts and impregnations. Numerous reviews of Fe–Mn deposit genetic

processes and distributions exist (Halbach et al., 1981; Aplin and Cronan, 1985; Halbach et al., 1988; Hein et al., 1997, 2000, 2013; Hein and Koschinsky, 2013). These deposits are classified in three main categories: hydrogenetic, diagenetic and hydrothermal (Bonatti et al., 1972; Hein et al., 1997; Bau et al., 2014; Schmidt et al., 2014) and are commonly discriminated by using characteristic variations of Fe, Mn, Cu, Ni, and Co contents.

Crusts form by hydrogenetic precipitation of colloidal particles of Fe and Mn oxyhydroxides onto rock substrates (Dymond et al., 1984; Bau et al., 1996; Hein et al., 2000; Schultz, 2006). Hydrogenetic crusts concentrate some trace metals (Co, Ni, Ti, HFSE and REY) at many orders of magnitude above their concentration in seawater (Bau et al., 1996; Hein and Koschinsky, 2013), which is promoted by the high reaction

\* Corresponding author at: University of Southampton, National Oceanography Centre, Ocean and Earth Sciences, Waterfront Campus, European Way, Southampton SO14 3ZH, Hampshire, UK.

E-mail address: [pmj1e13@soton.ac.uk](mailto:pmj1e13@soton.ac.uk) (P. Josso).

surface area of Fe-Mn oxyhydroxides (average of 325 m<sup>2</sup>/g for bulk  $\delta$ -MnO<sub>2</sub> and FeOOH) (Hein and Koschinsky, 2013; Pourret and Davranche, 2013), slow oxidation reaction kinetics, and slow growth rates (Bau et al., 1996). Polymetallic nodules constitute mixed-source deposits formed by hydrogenetic and/or diagenetic precipitation of Fe-Mn colloids around a nucleus on the surface of soft sediments. Interactions of both hydrogenetic and diagenetic processes lead to a range of bulk Mn/Fe ratios from 1 to 2.5 for oxic diagenesis and up to 50 when the sedimentary column is suboxic near the seabed (Calvert and Piper, 1984; Schultz, 2006). Metals (Ni, Cu and Co), REY and HFSE in nodules are mainly derived from seawater through hydrogenetic precipitation and further enrichment in metallic elements (Mn, Cu, Ni and Zn) occurs via diagenetic precipitation (Ohta et al., 1999).

Hydrothermal Fe-Mn deposits form under various conditions of temperature and geological settings; (i) plume fall-out deposits associated with high temperature venting (Bonatti, 1975; Corliss et al., 1978; Barret et al., 1987; German et al., 2002) form when particles derived from hydrothermal solutions precipitate during mixing with cold oxidizing seawater and settle on the seafloor forming the well-known metalliferous sediments encountered near hydrothermal fields such as along the East Pacific rise (EPR) or the Mid-Atlantic Ridge (MAR) (Barret and Jarvis, 1988; Goulding et al., 1998). Enrichment of metals, REY and other critical elements in oxyhydroxides occurs by sorption from seawater onto colloids in seawater and on the surface of crusts and nodules after accretion of the colloids. (ii) Diffuse hydrothermal systems are usually associated with off-axis hydrothermal circulation along MOR and within submarine volcanoes along volcanic arcs and hot spot seamounts, or less commonly associated with fractures distant from oceanic ridges (Hein et al., 2008b; Edwards et al., 2011). They form stratabound layers and crusts, and cement the sediment column with either Fe or Mn oxides by fluids percolating within porous sediment, pyroclastic deposits, and volcanic breccias (Fouquet et al., 1993). These deposits show a distinct mineralogy and texture from hydrogenetic crusts (Burgath and Von Stackelberg, 1995; Schultz, 2006). Fe-Mn hydrothermal deposits exhibit a wide range of Mn/Fe ratios from 0.001 (nearly no Mn) up to 4000, as a function of fluid temperature and redox conditions (Burgath and Von Stackelberg, 1995; Schultz, 2006). The rapid precipitation of these hydrothermal oxides commonly forms deposits with low minor metal contents; those influenced by hydrogenetic precipitation show an intermediate composition.

In 2010 an Ifremer mission exploring the mineral resources potential of the Wallis and Futuna archipelago (SW Pacific) dredged Fe-Mn hydrothermal samples showing the strongest metal enrichments recorded in Fe-Mn oceanic deposits (Pelleter et al., 2017). Hence the discovery of these metal-rich low temperature (LT) hydrothermal deposits requires explanation of (i) their mode of formation, (ii) the associated fluid geochemistry, and (iii) their economic potential as an oceanic resource, as well as (iv) the way we classify and discriminate Fe-Mn oceanic Fe-Mn deposits. Although we present bulk geochemical and mineralogical results for these unusual deposits, the first questions are presented elsewhere (Pelleter et al., 2017). We develop here how these deposits challenge our way of classifying Fe-Mn oceanic deposits and explore new geochemical tools for their discrimination.

## 2. Material and methods

### 2.1. Material

Hydrothermal samples were recovered during an Ifremer research cruise in the French exclusive economic zone (EEZ) of Wallis and Futuna in August 2010. The area studied is bordered by the North Fiji fracture zone, the active Tonga and Vanuatu subduction zones and associated Lau and North Fiji back-arc basins, and the currently active Samoan hotspot. Several extensional zones were recognized (Pelletier et al., 2001; Fouquet et al., 2015) including the Futuna and Alofi ridges and an area formed by a complex system of diffuse magmatism with

multiple volcanic edifices. Three atypical low-temperature Fe-Si-Mn deposits were discovered during the cruise aboard R/V Atalante, Utu Uli, Anakele, and Utu Segá (Fig. 1) from which samples were collected by dredging and HOV dive operations. The deposits found at Utu Uli and Anakele occur as massive, dense and laminated crusts of Mn oxyhydroxides from the summit of volcanic edifices composed of pyroclastic material, pillow lavas and more rarely sediments. Locally, the Mn crusts are crosscut by Fe-Si precipitates displaying ridge or vein-like structures up to 1 m high (Pelleter et al., 2017). The mineralization extends below these crusts as Mn oxyhydroxides, Fe oxides and nontronite cementing basaltic pyroclastic facies and brecciated lavas (Pelleter et al., 2017). Crusts have been observed covering three distinct volcanic edifices in the Utu Uli area representing an approximate area of 1.5 km<sup>2</sup> with thicknesses up to 5 cm, whereas sediment accumulation at the other sites prevented estimation of the extent of the deposits. No hydrothermal discharge was observed in the vicinity of the three sites. The present study focuses on 16 samples recovered from dredge hauls showing a range of composition from nearly pure Mn oxide to mixed Mn-Fe ± Si compositions. Sample FU-DR01-03 was later subdivided in three subsamples of oxides from the impregnated host sediment, an internal layer of the crust and the surface layer. See Pelleter et al. (2017) for bulk composition.

### 2.2. Methods

Mineralogical identification was made through X-ray diffraction (XRD) at Ifremer using a BRUCKER AXS D8 Advance (with Bragg-Bentano goniometer and VANTEC-1 positive sensitive detector – PSD) and BRUCKER AXS D2 Phaser. Prior to analysis, samples were dried at 60 °C and milled with agate mortar then deposited on a XRD sample holder and flattened with a glass slide. Samples were analyzed using Cu-K $\alpha$  radiation over 2 $\theta$  ranging from 2° to 70° at 40 kV and 30 mA. Additional analyses were made to characterize clay minerals (Pelleter et al., 2017). Minerals were identified using Eva search-match software.

Bulk chemical composition of each sample was determined. Samples were ground to a powder (90% of particles <80  $\mu$ m) using an agate pestle and mortar. Major elements and selected trace elements were analyzed by X-ray fluorescence with a BRUCKER AXS S8 Tiger automated XRF spectrometer on pressed pellets (Pelleter et al., 2017).

Additional trace elements (Sr, Y, Zr, Nb, Th, and REE) were analyzed by inductively coupled plasma mass spectrometry using an ELEMENT II magnetic field ICP-MS at Institut Universitaire Européen de la Mer (IUEM) in Brest. The dissolution procedure was as follows; 0.1 g of sample powder was digested in a Teflon bottle with 4 mL of 6 mol/L hydrochloric acid for 24 h on a hot plate (120 °C) with a Tm spike. If present, the residual phase composed of mostly silicates and refractory minerals was then extracted by centrifuge and digested by a mixture of hydrofluoric and hydrochloric acid (3:1) for 48 h on a hot plate (120 °C), evaporated and then remixed with the previously digested phase. The solution (0.5  $\mu$ L) was then evaporated on a hot plate and the residue was made up to 10 mL with a 2% nitric and 0.05% hydrofluoric acid solution for trace element analysis by ICP-MS. Data were corrected using internal calibrations, BHVO-2 standard, and a Tm spike correction (Barrat et al., 1996). Concentrations are expressed as % for weight %.

The rare earth and yttrium (REY) are discussed separately from the HFSE group for ease of description of their geochemical behavior and fractionation into Fe-Mn oceanic deposits although most lanthanides are HFSE from a geochemical point of view apart for Eu in its divalent state which is considered a large ion lithophile element (LILE). The Ce and Eu anomalies (Ce/Ce\* and Eu/Eu\*) are calculated as the ratio of the normalized values (subscript n) of an element by the interpolation of the adjacent elements (superscript \*) such that;

$$\text{Ce/Ce}^* = \frac{\text{Ce}_n}{\sqrt{(\text{La}_n * \text{Pr}_n)}}$$

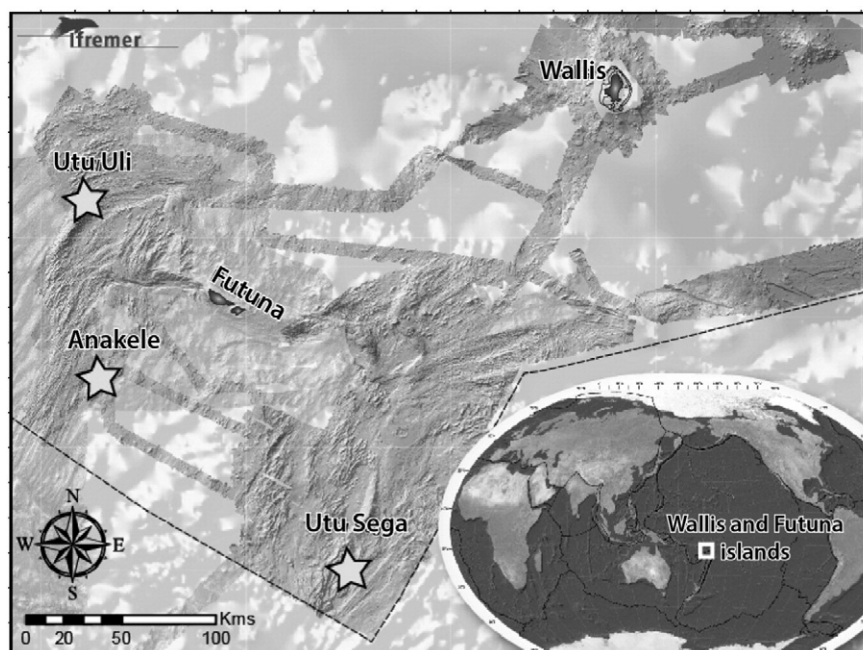


Fig. 1. Wallis and Futuna map showing the position of the main hydrothermal mounds (stars) discovered during Ifremer's cruises.

and

$$\text{Eu}/\text{Eu}^* = \frac{\text{Eu}_n}{\sqrt{(\text{Sm}_n * \text{Gd}_n)}}$$

Note that all following data of this study have been calculated using normalization to chondritic values, and normalization to Post-Archean Australian Shale (PAAS, Taylor and McLennan (1985)) is used for calculation of normalized Y/Ho ratio (Bau et al., 2014).

Pearson coefficient correlation matrix was calculated on the data set ( $n = 18$ ) to observe correlated geochemical variations and extract information on possible phase associations during precipitation.  $\text{SiO}_2$ ,  $\text{Al}_2\text{O}_3$ , Fe, Mn, CaO, MgO,  $\text{TiO}_2$ ,  $\text{P}_2\text{O}_5$ , Co, Ni, Cu, Y, Zr, La, Ce, Eu, Yb, Ce/Ce\*, Eu/Eu\* and total REE content ( $\Sigma\text{REE}$ ) were taken into account. As geochemical concentrations for each element do not follow a normal distribution, results are later reported as the median with a 95% confidence level.

### 3. Results

#### 3.1. Mineralogy

Bulk X-ray diffraction on the massive surface layer displaying a metallic grey luster shows birnessite and todorokite, 7 Å and 10 Å manganates respectively (Pelleter et al., 2017). The presence of vernadite (poorly crystalline  $\delta\text{-MnO}_2$ ) is suspected but could not be confirmed due to the overlap of reflections with birnessite and todorokite. Iron oxides are dominated by amorphous oxyhydroxides, with the presence of discrete goethite grains. Nontronite, the ferrous end-member of dioctahedral smectite, forms the cement for and replaces pyroclastic rocks onto which the Mn oxide layers developed.

#### 3.2. Bulk geochemistry

Bulk sample composition is dominated by Mn ( $40.5 \pm 3.6\%$ ),  $\text{SiO}_2$  ( $3.5 \pm 2.6\%$  including 5 outliers ranging from 12.4 to 16.7%) and Fe ( $3.0 \pm 2.2\%$  including 4 outliers ranging from 10 to 16.5%), with Mn/Fe ratio ranging from 1.6 to 3929 (Table 1). Other major elements decrease in abundance as follows;  $\text{Na}_2\text{O}$  ( $4.4 \pm 0.4\%$ ), MgO ( $2.5 \pm 0.4\%$ ),

CaO ( $1.75 \pm 1.0\%$ ),  $\text{Al}_2\text{O}_3$  ( $0.64 \pm 0.5\%$ ) and  $\text{TiO}_2$  ( $0.05 \pm 0.04\%$ ). Focus metal contents of some samples are anomalously high in comparison with typical hydrothermal Fe-Mn deposit metal concentrations (Hein et al., 1997), with  $0.72 \pm 0.7\%$  Ni,  $0.35 \pm 0.3\%$  Co and  $0.15 \pm 0.2\%$  Cu, with maximum values of 4.7% Ni, 2.2% Co and 1.5% Cu (Table 1). This enrichment in potential economic metals is unusual for LT hydrothermal deposits and suggests the absence of sulphide precipitation at depth at higher pressure and temperature conditions, which usually scavenge most of the Ni and Cu. These deposits might constitute the distal end-member of high temperature systems whereby metals were transported in a fluid with high oxygen fugacity. Continuous mixing with seawater lead to the precipitation of Fe and Mn oxides, rapidly scavenging transported metals (Pelleter et al., 2017). Other trace elements fall into the expected range of concentrations for LT Fe-Mn hydrothermal deposits; Sr ( $329 \pm 37$  ppm), Y ( $18 \pm 4$  ppm) and Zr ( $5.3 \pm 3$  ppm, excluding sample FU-DR15-06 with 85 ppm Zr).

REE concentrations in these hydrothermal samples are low ( $\Sigma\text{REE} = 26.1 \pm 11.5$  ppm), with a maximum content of 126 ppm REE in sample FU-DR15-06 associated with the highest concentration in  $\text{P}_2\text{O}_5$  (0.43%) and Zr. Normalized REE trends (Fig. 2) show two distinctive signatures. One group includes all samples from dredge FU-DR22, while the second group includes the rest of the hydrothermal sample set. This latter group displays marked light-REE (LREE) enrichment with regards to middle-REE (MREE);  $\text{La}_{\text{CH}}/\text{Sm}_{\text{CH}}$  varies from 2.98 to 7.02 and  $\text{Gd}_{\text{CH}}/\text{Yb}_{\text{CH}}$  ratios from 0.88 to 1.20. Most patterns display a negative Eu anomaly (0.67–0.98) and Ho and Er enrichment forming the top of a smooth convex-up pattern on the HREE. On the other hand, samples from core FU-DR22 have approximately flat LREE-MREE patterns ( $\text{La}_{\text{CH}}/\text{Sm}_{\text{CH}} = 0.83\text{--}1.52$ ) with distinct heavy-REE (HREE) enrichment; average  $\text{Gd}_{\text{CH}}/\text{Yb}_{\text{CH}} = 0.47$ . A marked positive Eu anomaly is present as well as both positive and negative Ce anomalies for different samples. The  $\text{Y}_{\text{PAAS}}/\text{Ho}_{\text{PAAS}}$  ratio for these hydrothermal samples varies from 0.66 to 1.37, regardless of the REE pattern, showing a depletion in Y relative to shale for many of those samples. This signature is thought to represent precipitation of oxides from a fluid close to seawater composition (Bau et al., 2014; Schijf et al., 2015). High temperature hydrothermal fluids associated with vent systems usually show well-developed positive Eu anomalies (Michard, 1989; Bau, 1991; Douville et al., 1999;

**Table 1**  
Geochemical data for hydrothermal samples from Wallis and Futuna.

Sample	Si	Al	Fe	Mn	Ca	Mg	K	Na	Ti	P	Mn/Fe	Cu + Co + Ni	Co	Ni	Cu	Zn	As	Rb	Sr	Y	Zr	Nb	Cs	Ba	La	Ce	Pr	
	wt.%	wt.%	wt.%	wt.%	wt.%	wt.%	wt.%	wt.%	wt.%	wt.%		wt.%	ppm	ppm	ppm	ppm	ppm	ppm	ppm	ppm	ppm	ppm	ppm	ppm	ppm	ppm	ppm	
	XRF	XRF	XRF	XRF	XRF	XRF	XRF	XRF	XRF	XRF			XRF	XRF	XRF	XRF.....	ICP-MS	ICP-MS	ICP-MS	ICP-MS	ICP-MS	ICP-MS	ICP-MS	ICP-MS	ICP-MS	ICP-MS	ICP-MS	
Hydrothermal crusts – Wallis & Futuna																												
FU-DR01-01	1.75	0.44	3.40	42.42	0.83	1.21	0.63	3.99	0.06	0.05	12.49	4.79	1552	46,129	200	206	31	6	197	22	4	0.52	0.04	448	10.1	2.5	1.8	
FU-DR01-03	2.39	0.12	3.10	45.18	1.78	0.58	0.35	3.97	0.02	0.04	14.56	0.32	1510	1687	41	<5	17	4	278	7	4	0.29	0.07	141	3.6	1.4	0.6	
FU-DR01-03 C	1.07	0.10	1.19	48.65	1.15	1.66	0.63	2.34	0.02	0.03	40.93	0.95	1191	8204	67	51	–	–	347	11	3	0.23	0.05	518	4.6	0.9	0.6	
int																												
FU-DR01-03	1.20	0.09	1.30	49.91	1.81	0.62	0.24	3.19	0.02	0.03	38.41	0.43	2232	1962	69	30	–	–	329	9	6	0.42	0.07	301	5.3	4.4	0.9	
Hydt																												
FU-DR01-03	7.81	0.33	10.03	31.31	0.99	1.54	0.90	2.20	0.04	0.08	3.12	1.32	1086	12,084	69	150	–	–	–	–	–	–	–	–	–	–	–	
Imp																												
FU-DR01-04	6.33	0.42	11.57	27.07	1.02	1.54	0.71	2.83	0.06	0.12	2.34	1.80	494	17,435	115	113	80	12	236	19	19	1.33	0.21	230	7.8	4.1	1.2	
FU-DR01-06	0.41	0.12	0.65	52.01	0.83	1.03	0.83	4.19	0.03	0.03	80.00	4.93	2428	46,666	249	135	14	6	279	23	3	0.44	0.02	651	13.5	0.9	1.7	
FU-DR01-07	1.83	0.18	3.48	44.33	1.00	1.06	0.76	3.68	0.03	0.04	12.74	4.44	22,371	20,942	1041	54	31	6	289	18	2	0.42	0.04	905	10.8	1.9	1.5	
FU-DR01-08	1.59	0.19	3.20	43.07	0.77	1.03	0.71	4.19	0.03	0.04	13.45	4.93	4431	44,705	163	120	26	6	536	9	5	0.18	0.09	2509	3.5	3.3	0.7	
FU-DR15-05	1.64	0.15	2.85	39.74	1.29	1.53	0.85	2.88	0.02	0.05	13.94	3.65	13,267	7866	15,329	414	43	7	416	20	9	0.64	0.04	1121	11.6	5.1	1.7	
FU-DR15-06	5.79	0.87	16.48	25.80	1.44	1.71	0.85	2.18	0.11	0.19	1.57	1.27	488	10,184	2013	724	129	9	405	43	85	4.71	0.13	637	32.7	24.3	5.8	
FU-DR15-09	6.15	0.82	12.01	27.93	1.22	1.66	0.99	2.28	0.06	0.11	2.33	1.93	1309	6380	11,650	468	65	10	308	16	26	1.28	0.12	816	8.3	6.9	1.8	
FU-DR15-10	1.63	0.21	3.50	42.06	1.11	1.29	0.78	3.52	0.03	0.04	12.03	3.06	9040	6297	15,305	256	21	6	267	12	5	0.34	0.05	740	5.2	2.7	1.2	
FU-DR22-02	0.33	0.45	0.21	41.18	2.69	1.80	0.68	3.14	0.03	0.02	196.38	1.69	9686	2909	4333	118	9	4	362	13.5	5.0	<5	48	309	1.1	1.4	0.3	
FU-DR22-03	7.80	2.62	1.68	29.38	5.76	2.64	0.46	2.94	0.29	0.04	17.44	1.12	6800	1297	3066	91	6	3	285	17.5	16.0	<5	40	104	1.5	5.7	0.6	
FU-DR22-04	0.78	0.70	0.31	38.26	4.31	1.65	0.38	3.30	0.05	0.03	121.64	1.94	12,304	2298	4806	112	12	3	399	21.1	5.5	<5	38	434	1.7	4.6	0.5	
FU-DR22-05	0.10	0.35	0.01	39.29	1.46	1.79	0.66	3.33	0.01	0.02	3929.1	1.98	8331	6569	4933	506	9	3	360	22.5	3.2	<5	41	262	1.6	1.6	0.4	
FU-DR22-06	0.70	0.67	0.57	36.35	5.53	1.47	0.32	3.32	0.04	0.03	63.41	1.79	11,254	2175	4475	97	14	3	421	22.4	6.0	<5	43	255	2.0	4.6	0.5	

**Table 1** (continued)

Sample	Nd	Sm	Eu	Gd	Tb	Dy	Ho	Er	Yb	Lu	Hf	Ta	Th	Li	Sc	V	Cd	Pb	Ce/Ce*	Eu/Eu*	Σ REE	(La/Sm)n	(Gd/Yb)n	(Y/Ho)PAAS	
	ppm	ppm	ppm	ppm	ppm	ppm	ppm	ppm	ppm	ppm	ppm	ppm	ppm	ppm	ppm	ppm	ppm	ppm			ppm				
	ICP-MS	ICP-MS	ICP-MS	ICP-MS	ICP-MS	ICP-MS	ICP-MS	ICP-MS	ICP-MS	ICP-MS	ICP-MS	ICP-MS	ICP-MS	ICP-MS	ICP-MS	ICP-MS	ICP-MS	ICP-MS							
Hydrothermal crusts – Wallis & Futuna																									
FU-DR01-01	8.4	1.5	0.5	2.2	0.3	2.4	0.6	1.9	1.7	0.3	0.1	0.0	0.1	270.3	398	64	0.68	2.69	0.14	0.79	36	4.26	1.05	1.14	
FU-DR01-03	2.6	0.5	0.1	0.7	0.1	0.9	0.2	0.7	0.6	0.1	0.1	–	0.0	46.2	424	21	0.49	1.90	0.23	0.70	13	4.55	0.95	1.02	
FU-DR01-03 C	2.8	0.5	0.1	0.8	0.1	1.0	0.3	0.8	0.7	0.1	0.0	–	0.0	345.1	0.2	55	0.60	2.38	0.12	0.69	14	5.81	0.91	1.37	
int																									
FU-DR01-03	4.0	0.8	0.2	1.1	0.2	1.2	0.3	0.9	0.8	0.1	0.1	–	0.3	53.1	0.3	50	0.08	4.77	0.48	0.72	21	4.18	1.10	1.03	
Hydt																									
FU-DR01-03	–	–	–	–	–	–	–	–	–	–	–	–	–	–	–	–	–	–	–	–	–	–	–	–	
Imp																									
FU-DR01-04	5.5	1.1	0.3	1.7	0.3	1.9	0.5	1.6	1.5	0.2	0.3	0.0	0.2	401.9	2143	63	0.49	6.31	0.33	0.70	29	4.54	0.89	1.26	
FU-DR01-06	7.6	1.2	0.4	2.1	0.3	2.5	0.7	2.2	1.9	0.3	0.0	0.0	0.0	368.9	347	70	1.08	1.40	0.04	0.71	37	7.02	0.89	1.06	
FU-DR01-07	7.0	1.1	0.3	1.6	0.2	1.7	0.5	1.5	1.1	0.2	0.1	0.0	0.0	559.8	328	46	0.85	2.20	0.11	0.69	31	6.01	1.14	1.25	
FU-DR01-08	3.4	0.7	0.3	1.1	0.2	1.1	0.3	0.8	0.8	0.1	0.1	–	0.0	29.3	703	79	0.42	57.14	0.49	0.90	17	2.98	1.12	1.03	
FU-DR15-05	8.0	1.6	0.5	2.8	0.5	3.1	0.8	2.4	2.4	0.4	0.1	0.0	0.1	441.6	703	133	6.36	3.89	0.27	0.69	43	4.43	0.92	0.84	
FU-DR15-06	25.3	5.2	1.4	6.8	1.1	7.1	1.6	4.8	4.6	0.7	1.1	0.1	0.5	272.9	4595	166	1.19	36.54	0.43	0.71	126	3.93	1.20	0.87	
FU-DR15-09	8.2	1.6	0.4	2.2	0.4	2.4	0.6	1.9	1.9	0.3	0.4	0.0	0.2	208.3	3944	101	1.74	7.66	0.43	0.70	39	3.17	0.96	0.82	
FU-DR15-10	5.4	1.0	0.3	1.5	0.2	1.6	0.5	1.5	1.4	0.2	0.1	0.0	0.0	512.5	772	87	1.40	2.33	0.26	0.66	24	3.21	0.88	0.84	
FU-DR22-02	1.5	0.5	0.3	0.9	0.2	1.7	0.5	1.8	2.1	0.4	–	–	<5	–	–	–	–	<5	0.59	1.48	14	1.52	0.35	0.87	
FU-DR22-03	3.2	1.1	0.5	1.8	0.3	2.6	0.6	1.9	2.0	0.3	–	–	<5	–	–	–	–	<5	1.47	1.18	24	0.83	0.72	0.91	
FU-DR22-04	2.5	0.8	0.6	1.5	0.3	2.9	0.8	2.8	3.2	0.6	–	–	<5	–	–	–	–	<5	1.23	1.56	26	1.32	0.39	0.83	
FU-DR22-05	2.6	1.0	0.8	2.0	0.5	4.0	1.1	3.5	3.6	0.6	–	–	<5	–	–	–	–	8	0.47	1.72	27	1.07	0.47	0.66	
FU-DR22-06	2.8	0.9	0.6	1.6	0.3	2.9	0.8	2.7	3.0	0.5	–	–	<5	–	–	–	–	<5	1.06	1.47	26	1.45	0.43	0.92	



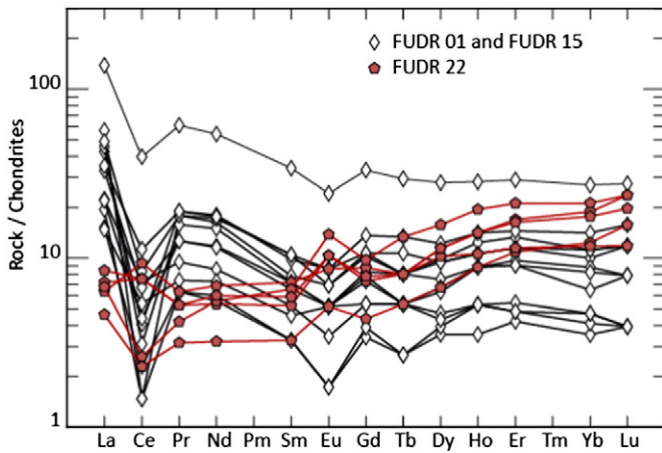


Fig. 2. Chondrite-normalized REE patterns of hydrothermal samples from Wallis and Futuna EEZ.

Craddock et al., 2010). Consequently, REE trends from Utu Segá samples (FU DRR 22) with small positive  $\text{Eu}^*$  anomalies reflect a greater influence of a HT fluid than at the two other sites.

The correlation coefficients (Table 2;  $n = 18$ ) can be explained in terms of mineralogical control for most major elements. Iron and Si are strongly fractionated from Mn during precipitation as Fe and Si precipitate under slightly reducing conditions to form nontronite, or amorphous silica and Fe oxyhydroxides as highlighted by the strong correlation of Fe and  $\text{SiO}_2$  (0.75). On the other hand, Mn forms oxyhydroxides at the seawater-sediment interface or impregnations within the volcanoclastic-sedimentary pile under oxidizing conditions, showing a negative correlation with Fe (−0.72) and Si (−0.80). Mn is negatively correlated to  $\text{MgO}$ ,  $\text{P}_2\text{O}_5$ , Zr and Ce (−0.63 to −0.72). Aluminum is strongly positively correlated to  $\text{TiO}_2$  (0.96), CaO and  $\text{MgO}$  ( $r > 0.7$ ). Copper, Ni and Co do not show significant correlations (−0.5 <  $r$  < 0.3) with elements considered here and behave independently from each other in this sample set.  $\text{P}_2\text{O}_5$  correlation with Fe (0.96) is consistent with phosphate sorption onto Fe oxyhydroxides in hydrothermal systems (Edmonds and German, 2004). Among HFSE and REY, all are positively correlated to  $\text{P}_2\text{O}_5$  (0.62 to 0.90), except Yb which does not show significant correlations (0.39). The total REE content ( $\Sigma\text{REE}$ ) correlates positively with  $\text{P}_2\text{O}_5$  and Fe (0.82 and 0.69 respectively) and not significantly to Mn (−0.48), suggesting that minor scavenging from open seawater occurred during formation of the Mn crusts with REE mainly derived from the LT hydrothermal fluids.

## 4. Discussion

### 4.1. Classification and alternatives

Fe–Mn deposits have typically been classified using the Bonatti ternary diagram (Bonatti et al., 1972) using major chemical characteristics (Fe, Mn, Cu–Ni–Co) to discriminate them. Our hydrothermal samples scatter on the Mn–(Co + Cu + Ni) side of the diagram as a result of the unusual metal enrichments which places them outside of the originally identified hydrothermal field (Fig. 3) (Bonatti et al., 1972). Some samples have even higher minor metal contents than the polymetallic nodules. Nevertheless, apart from the atypical Ni–Co–Cu enrichments of these deposits, samples from Wallis and Futuna are similar in composition and mineralogy to LT hydrothermal deposits collected in the Gulf of Aden (Cann et al., 1977), the Mediterranean Sea (Dekov et al., 2009), the Mid-Atlantic Ridge (Mills et al., 2001; Severmann et al., 2004) and the Pacific Ocean (Corliss et al., 1978; Alt, 1988; Fouquet et al., 1993; Hein et al., 1996, 2008b; Kuhn et al., 2003; Fitzgerald and Gillis, 2006; Sun et al., 2012; Zeng et al., 2012).

Table 2  
Pearson coefficient correlation matrix for hydrothermal samples from Wallis and Futuna ( $n = 18$ ).

	$\text{SiO}_2$	$\text{Al}_2\text{O}_3$	Fe	Mn	CaO	MgO	$\text{TiO}_2$	$\text{P}_2\text{O}_5$	Co	Ni	Cu	Y	Zr	La	Ce	Eu	Yb	Ce/Ce*	Eu/Eu*
$\text{Al}_2\text{O}_3$	0.568735																		
Fe	0.747663	0.100589																	
Mn	−0.79544	−0.58987	−0.72652																
CaO	0.051305	0.698972	−0.34959	−0.25225															
MgO	0.436206	0.767908	0.111644	−0.63126	0.503977														
$\text{TiO}_2$	0.623521	0.967027	0.150492	−0.53246	0.576407	0.694079													
$\text{P}_2\text{O}_5$	0.664924	0.161775	0.960537	−0.72197	−0.25872	0.155431	0.215378												
Co	−0.39322	−0.00576	−0.43934	0.157463	0.29228	0.081866	−0.06573	−0.40203											
Ni	−0.14988	−0.27626	0.004443	0.303373	−0.50157	−0.33983	−0.16238	−0.00873	−0.17982										
Cu	−0.06702	0.0394	0.006447	−0.18411	0.041681	0.237914	−0.04129	0.346705	−0.35753	−0.06573									
Y	0.221157	0.250393	0.472955	−0.49285	0.074076	0.354644	0.242684	0.625055	0.08207	0.00369	−0.0002								
Zr	0.252892	0.309583	0.797846	−0.64316	−0.04674	0.280181	0.345846	0.901268	−0.1282	0.009769	0.741298	0.758344							
La	0.28386	−0.04971	0.682528	−0.27257	−0.38722	−0.05875	0.061285	0.78364	−0.21258	−0.03913	0.244949	0.755922	0.822937						
Ce	0.461612	0.321525	0.717067	−0.60877	0.052211	0.252436	0.348961	0.837461	−0.15874	0.049042	0.15874	0.755922	0.973839	0.799314					
Eu	0.257957	0.372293	0.455706	−0.57419	0.175507	0.437783	0.331438	0.600485	−0.03183	0.1056	0.080356	0.917156	0.794824	0.646561	0.83314				
Yb	0.084553	0.317537	0.256953	−0.52591	0.319181	0.503891	0.207125	0.394881	0.117808	−0.22235	0.220391	0.860125	0.59099	0.425281	0.639921	0.921624			
Ce/Ce*	0.227307	0.760726	−0.18772	−0.42883	0.916921	0.593823	0.636615	−0.13081	0.196981	−0.46071	0.052749	0.09114	0.051195	0.156456	0.639921	0.26731	0.379188		
Eu/Eu*	−0.26706	0.298811	−0.44734	−0.13368	0.631802	0.457778	0.110786	−0.3969	0.330377	−0.31895	0.003643	0.116292	−0.2093	−0.49765	−0.14567	0.269953	0.517461	0.668989	
$\Sigma$ REE	0.345145	0.158285	0.693932	−0.48263	−0.14926	0.167058	0.207963	0.819019	−0.17535	0.051819	0.053767	0.87873	0.926843	0.935918	0.931109	0.859331	0.67695	−0.08988	−0.22656

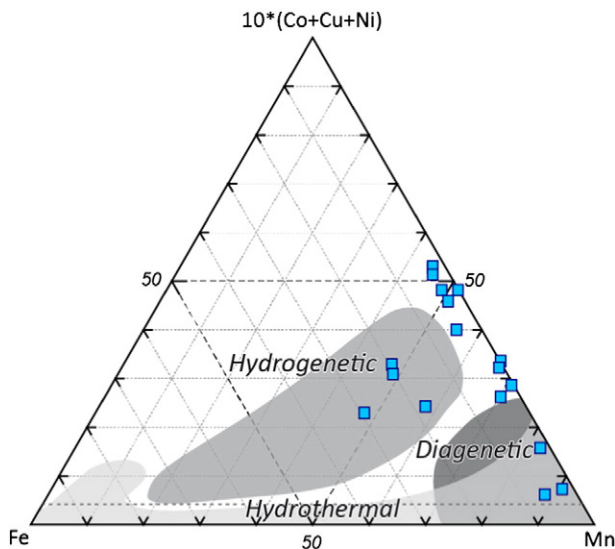


**Fig. 3.** Ternary discrimination system of hydrothermal samples from Wallis and Futuna. Note the abnormal distribution of samples away from the hydrothermal field due to unusual metal enrichments. After Bonatti et al. (1972).

In addition to the problem posed by this set of samples from the Wallis and Futuna EEZ, the ternary classification of Bonatti et al. (1972) does not clearly discriminate Fe-Mn deposits formed by mixed genetic processes such as nodules with various hydrogenetic/diagenetic proportions, hydrothermally derived particles incorporated during hydrogenetic crust growth, and our hydrothermal samples. The issue for nodules was discussed previously (Halbach and Puteanus, 1988) and hydrogenetic, diagenetic, and mixed-typed were identified within the existing diagram.

Alternative classification systems have been proposed and discussed recently for the discrimination of Fe-Mn deposits. Other ways have been explored using exclusively major (Conly et al., 2011), or minor and trace elements (Choi and Hariya, 1992; Nicholson, 1992; Bau et al., 2014). Within a  $\text{MgO} \cdot 10 - \text{Fe}_2\text{O}_3 - \text{MnO}_2$  ternary diagram, Conly et al. (2011) described discriminating fields for oceanic and terrestrials Fe-Mn deposits. Despite some overlaps, this diagram allows sample separation due to the use of Mg as a discriminative feature for fluid chemistry; oceanic waters contain ~1200 ppm of Mg while end member hydrothermal fluids are considered Mg-free (Conly et al., 2011). However, considering LT hydrothermal and distal HT hydrothermal deposits, fluid chemistry for major elements is close to seawater composition. Hence this classification scheme is not well-suited for the compositional range found for oceanic Fe-Mn deposits, although it does separate marine and continental Mn-oxide deposits that are not mixed with Fe oxides.

Using trace-element mobility in hydrothermal fluids and seawater, Nicholson (1992) proposed a  $(\text{Co} + \text{Ni})$  vs  $(\text{As} + \text{Cu} + \text{Mo} + \text{Pb} + \text{V} + \text{Zn})$  binary diagram with distinction between hydrogenetic, diagenetic, or supergene and hydrothermal precipitation. Nodules and hydrogenetic crusts are well-discriminated on this diagram, however the unusually high Co and Ni contents of samples from Wallis and Futuna plot away from the designated hydrothermal field. A similar conclusion is reached for the classification proposed by Choi and Hariya (1992) using a Ni-Zn-Co ternary diagram. The binary discrimination diagrams of Bau et al. (2014) are based on Nd concentrations and fractionation of the geochemical twin Y and Ho against the Ce anomaly. These diagrams demonstrate the efficiency of REY as a discriminative feature for the various genetic types of marine Fe-Mn deposits. One of the most efficacious is the  $Y_{\text{PAAS}}/\text{Ho}_{\text{PAAS}}$  ratio, which if  $<1$  characterizes a hydrogenetic or diagenetic process. Hydrothermal deposits exhibit a wider range of ratios, mostly  $>1$  though a continuum

towards hydrogenetic ratios is observed representing the evolution of the exchange equilibrium between seawater and scavenging Fe-Mn oxides (Bau et al., 2014). Although really robust, this criterion cannot be used when considering hydrogenetic samples affected by phosphatisation due to a shift of the  $Y_{\text{PAAS}}/\text{Ho}_{\text{PAAS}}$  ratio to values as high as 1.8 (Asavin et al., 2010) (Fig. 4). We will therefore try to accommodate this characteristic of hydrogenetic samples within our discriminative diagrams including other common discriminative features of Fe-Mn deposits.

#### 4.2. New genetic discrimination diagrams

The objective of a new discrimination scheme therefore lies on the incorporation of new elements allowing the discrimination of hydrothermal samples from hydrogenetic and diagenetic deposits without relying solely on the metal content.

Fe-Mn deposits have long been known for their economic potential and accordingly most studies focused on the geochemistry of Fe, Mn, Cu, Ni and Co or a specific aspect of their trace element content with too few studies publishing a complete dataset including major, minor and trace elements. The published data used in the following plots were chosen to be representative of the diversity of Fe-Mn occurrences found throughout the deep ocean. Therefore data for polymetallic nodules include mixed hydrogenous-diatagenetic samples from the central and north eastern part of the Pacific Ocean ( $n = 149$ ) (Calvert and Price, 1977; Calvert and Piper, 1984; Dymond et al., 1984; Hein et al., 1997; Ohta et al., 1999; Węgorzewski and Kuhn, 2014), diagenetic nodules from the Peru basin ( $n = 31$ ) (Von Stackelberg, 1997), as well as samples from the Indian Ocean ( $n = 18$ ) (Pattan and Banakar, 1993; Balaram et al., 1995; Baturin and Dubinchuck, 2010). Data used for hydrogenetic crusts come from samples of the open Pacific Ocean ( $n = 72$ ) (De Carlo and Mc Murtry, 1992; Bau et al., 1996; Bau and Koschinsky, 2009; Asavin et al., 2010), including averaged compositions for diverse areas of the Pacific ( $n = 4$ ) (Hein et al., 1997), and samples from the Atlantic Ocean ( $n = 31$ ) (Baturin and Dubinchuck, 2011; Muñoz et al., 2013) and the Indian Ocean ( $n = 5$ ) (Surya Prakash et al., 2012). In addition to our own samples from Wallis and Futuna Archipelago, hydrothermal Fe-Mn samples from the literature include data from the Pacific Ocean: Mariana-Izu-Bonin Arc System ( $n = 6$ ) (Hein et al., 2008b), East Diamante Caldera ( $n = 6$ ) (Hein et al., 2014), Valu Fa Ridge system ( $n = 13$ ) (Sun et al., 2011), PACMANUS hydrothermal field ( $n = 18$ ) (Zeng et al., 2012), Baby bare seamount ( $n = 9$ ) (Fitzgerald and Gillis, 2006), Okhotsk Sea ( $n = 5$ ) (Baturin et al., 2010), metalliferous sediment and silica-hematite deposits of the Blanco Fracture Zone ( $n = 12$ ) (Hein et al., 2008a), ironstones from Central Pacific Seamounts ( $n = 3$ ) (Hein et al., 1994), and bacterially mediated metalliferous sediment from Loihi Seamount, Hawaii ( $n = 13$ ) (Edwards et al., 2011). Data for hydrothermal samples from the Atlantic Ocean include the ultramafic hosted deposits from the Mid Atlantic Ridge (MAR) ( $n = 8$ ) (Dekov et al., 2011). Finally, data from the Eolo Seamount in the Tyrrhenian sea ( $n = 22$ ) (Dekov et al., 2009) and the Indian ocean ( $n = 3$ ) (Surya Prakash et al., 2012) are considered. Mixed type samples of hydrogenous and hydrothermal origin from the Central Indian Ridge ( $n = 17$ ) (Kuhn et al., 1998; Takahashi et al., 2007) and the mercury- and silver-rich encrustation off the coast of California ( $n = 11$ ) (Hein et al., 2005) are included as well.

Major differences occur among Fe-Mn deposits when considering concentrations in high field strength elements such as Zr, Ti and the REY. Geochemical divergences for each mineral-forming process are illustrated in cross-plots (Fig. 4). Using characteristics of REY fractionation such as the Ce anomaly, one of the most distinctive features encountered in the various types of Fe-Mn deposits, the  $Y_{\text{PAAS}}/\text{Ho}_{\text{PAAS}}$  ratio (Bau et al., 2014), Zr or Ti content plotted against Mn/Fe ratio, and metal enrichments provide fairly good discrimination for each type of deposit. Relationships in Figs. 4 and 5 reflect the control of growth rates, precipitation kinetics, and pH conditions during

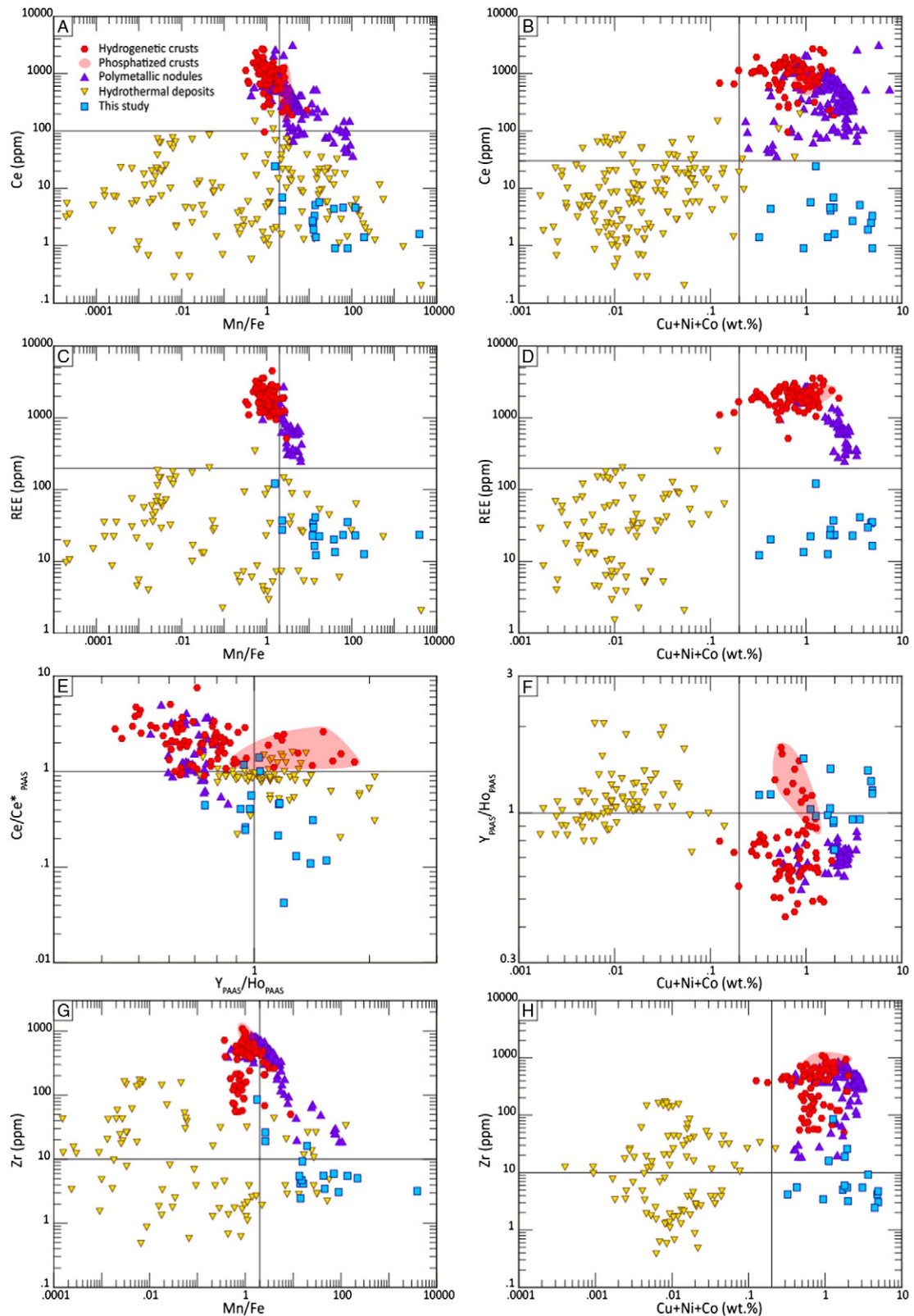


**Fig. 4.** Discrimination diagrams displaying HFSE concentrations, Ce anomalies and  $Y_{PAAS}/Ho_{PAAS}$  ratios (Bau et al., 2014) against changes in Mn/Fe ratios and potentially economic metals for oceanic Fe-Mn deposits.

mineral-forming processes and overall metal concentrations and trace element budget in the source fluid. The HFSE and REY are highly depleted in hydrothermal deposits (by one order of magnitude) and richer in hydrogenetic deposits, while polymetallic nodules of mixed hydrogenetic-diagenetic origin display more limited enrichments in

comparison with hydrogenetic deposits due to low contents of such elements in pore fluids. Hydrothermal deposit depletion in HFSE relates to the poor capacity of these elements to bind with the dominant chloride complex in hydrothermal fluids therefore implying a HFSE-depleted source fluid for Fe-Mn hydrothermal deposits (Douville et al., 2002).



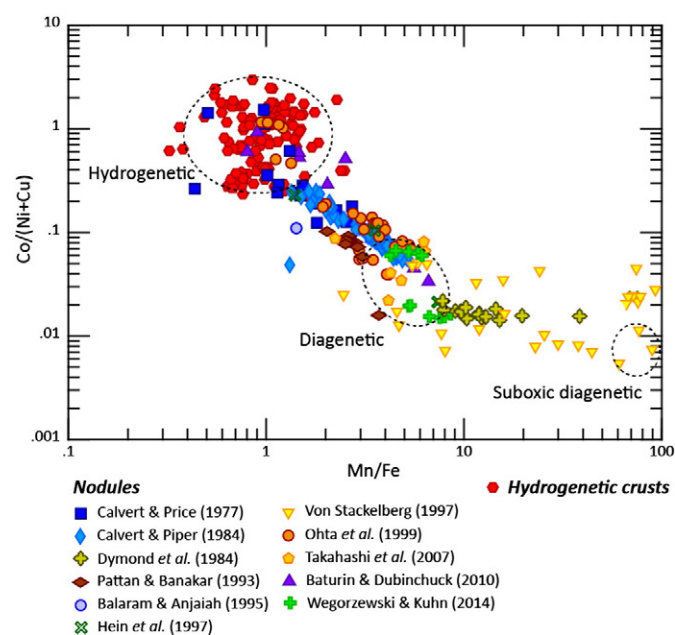


Fig. 5. Co/(Ni + Cu) vs Mn/Fe ratio diagram highlighting the relationship of hydrogenetic and diagenetic inputs to the composition of polymetallic nodules. See text for details on data used for hydrogenetic crusts. Oxic and suboxic diagenetic fields follow Dymond et al. (1984).

Furthermore, the fast precipitation of hydrothermal Fe-Mn deposits limits hydrogenetic enrichment of Zr, Ti and REY (Schmidt et al., 2014). In contrast, crusts and nodules growing at extremely slow rates benefit from extensive contact with seawater and pore fluids to scavenge dissolved trace metals. Of these two deposits, nodules display the largest range in composition considering Mn/Fe ratios and minor and trace element contents due to the influence of both diagenetic and hydrogenetic precipitation. As exemplified in Fig. 4, phosphatized samples of hydrogenetic crusts (Asavin et al., 2010) do not follow the discriminative features of the  $Y_{PAAS}/Ho_{PAAS}$  ratio (Bau et al., 2014) and these samples could not be distinguished from non-phosphatized crusts using other criteria (Ce, REE, and Zr).

The ratio of diagenetic to hydrogenetic input to nodules, and their associated minor metals, can be shown qualitatively by the Mn/Fe ratio. The higher the Mn relative to Fe, the higher is the diagenetic input. Nodules analyzed from the global ocean show that there is a continuum between the diagenetic and hydrogenetic end-members (Fig. 5). Metals (Ni, Cu, and Co), HFSE and REY in Fe-Mn deposits are mainly derived from seawater with hydrogenetic precipitation in Fe-Mn crusts and nodules. Further enrichment in elements such as Mn, Cu, Ni and Zn occurs during diagenesis whereby metals are released to pore fluids through the dissolution of the Mn oxyhydroxide fraction of the sediment releasing carried metals which become available to migrate up to the nodules at the oxic-suboxic interface (Ohta et al., 1999; Koschinsky et al., 2001). The diagenetic process does not link to Fe, Co, REY and HFSE enrichment in polymetallic nodules as Fe is mainly reprecipitated in the sediment as Fe oxyhydroxides or associated with silica to form nontronite (Calvert and Piper, 1984). Moreover, the limited mobility of Co, REY, and HFSE in interstitial waters compared to Cu, Ni, and Zn explains their relative enrichment in the most hydrogenetic samples and depletion with increasing diagenetic input (Jung and Lee, 1999; Ohta et al., 1999; Schultz, 2006; Baturin and Dubinchuck, 2009).

Therefore, Co, HFSE and REY enrichment in Fe-Mn deposits characterize hydrogenetic precipitation and it would be tempting to associate them in a new diagram to discriminate diagenetic and hydrothermal formation. However with unusual Co concentration averaging 0.6% and up to 2.2% in hydrothermal samples from Wallis and Futuna, it is

essential not to combine Co, HFSE and REY to separate metal-rich hydrothermal deposits from crusts and nodules.

#### 4.3. Incorporating REE and HFSE in a new classification scheme

The choice of elements to incorporate in a new discrimination diagram should accommodate variations in hydrogenous or diagenetic inputs to nodules, oxic/suboxic diagenesis in nodule bulk compositions, mixed hydrothermal-hydrogenetic formation, and metal-rich Fe-Mn hydrothermal deposits. We propose to use a first apex representing combined Fe and Mn concentrations  $(Fe + Mn)/4$  (wt.%), an index that represents the main constituent of Fe-Mn samples. The second apex represents the various metal enrichments produced by the three precipitation processes:  $10 * (Cu + Ni)$  in wt.%. Cobalt is deliberately left out of this apex as a common marker of hydrogenetic precipitation although its addition does not fundamentally change the positioning of samples, and could be considered in the case of extreme Co enrichment. HFSE and REY allow for the separation of hydrothermal samples from hydrogenetic and diagenetic deposits (Fig. 4). The last apex should therefore be formed by a combination of these elements. As studies of Fe-Mn deposits have not always presented complete minor and trace element data, we will focus on the most commonly published HFSE (e.g. Ti and Zr) and REY. The enrichment in REY and other HFSE is a function of growth rate, fluid source and chemistry, and also represents uptake of seawater complexes by Fe and Mn oxyhydroxides/oxides. Carbonates are the main complexing agent for REE;  $REE-CO_3^{+}$  and  $REE-CO_3^{-}$  account for at least 85% of REE ligands in seawater (Schijf et al., 2015), while Zr or Ti are dominantly complexed with hydroxides (Bruland, 1983; Bau et al., 1996) and enriched by surface complexation. Combining these elements that are fractionated by sorption on either Fe- or Mn-oxides has the objective of creating a restricted field for hydrogenetic precipitates in the diagram by including both scavenger phases and eliminates the influence of Mn/Fe ratios. Cerium constitutes probably the most efficient element among the REE series to use as a discriminative feature for Fe-Mn deposits. Indeed, Ce is easily hydrolyzed and continuously and irreversibly scavenged from seawater on the surface of Mn oxides (Takahashi et al., 2007) and positive Ce anomalies in Fe-Mn deposits are therefore regarded as typical of hydrogenetic precipitation. Owing to the differences in precipitation kinetics among the different Fe-Mn deposits and irreversible Ce uptake from seawater, this element will be most enriched in hydrogenetic deposits, lower in diagenetic deposits, and depleted in hydrothermal deposits.

Yttrium and La were also considered as these elements show strong enrichment in Fe-Mn deposits and are commonly analyzed in published studies. Combinations using Zr and Ce with either La or Y give similar results owing for the consistent fractionation of Y and La across the diverse environments of formation of Fe-Mn deposits. On the other hand, using an apex combining Zr, Y and La brings scatter in sample distribution. Notably, mixed-type deposits deviate from their predicted position between hydrothermal and hydrogenetic deposits. The absence of discrimination using La and Y relates to their common levels of enrichment in hydrogenetic and mixed hydrogenetic-hydrothermal deposits whereas using Ce brings more weight to the HFSE-REY apex. Indeed Ce will be strongly enriched (positive Ce anomaly) in purely hydrogenetic precipitate whereas the faster growth rate of mixed hydrogenetic-hydrothermal deposits (up to 29 mm/Ma) will prevent the formation of a positive Ce anomaly due to slow Ce oxidation kinetics (Kuhn et al., 1998). Consequently, using a combination of the most distinctive features of REE and HFSE behavior highlighted here, an apex with  $100 * (Zr + Y + Ce)$  in wt.% is a viable discriminant (Fig. 6).

In the resulting ternary diagram, hydrogenetic crust samples define a well-delineated group close to the HFSE and REY apex (Fig. 6A). These elements can be used as a marker for hydrogenetic input over diagenetic input, allowing discrimination of these contributions for polymetallic nodules that are otherwise ambiguous. Following the genetic classification of polymetallic nodules in Fig. 5 (Dymond et al., 1984), we observe



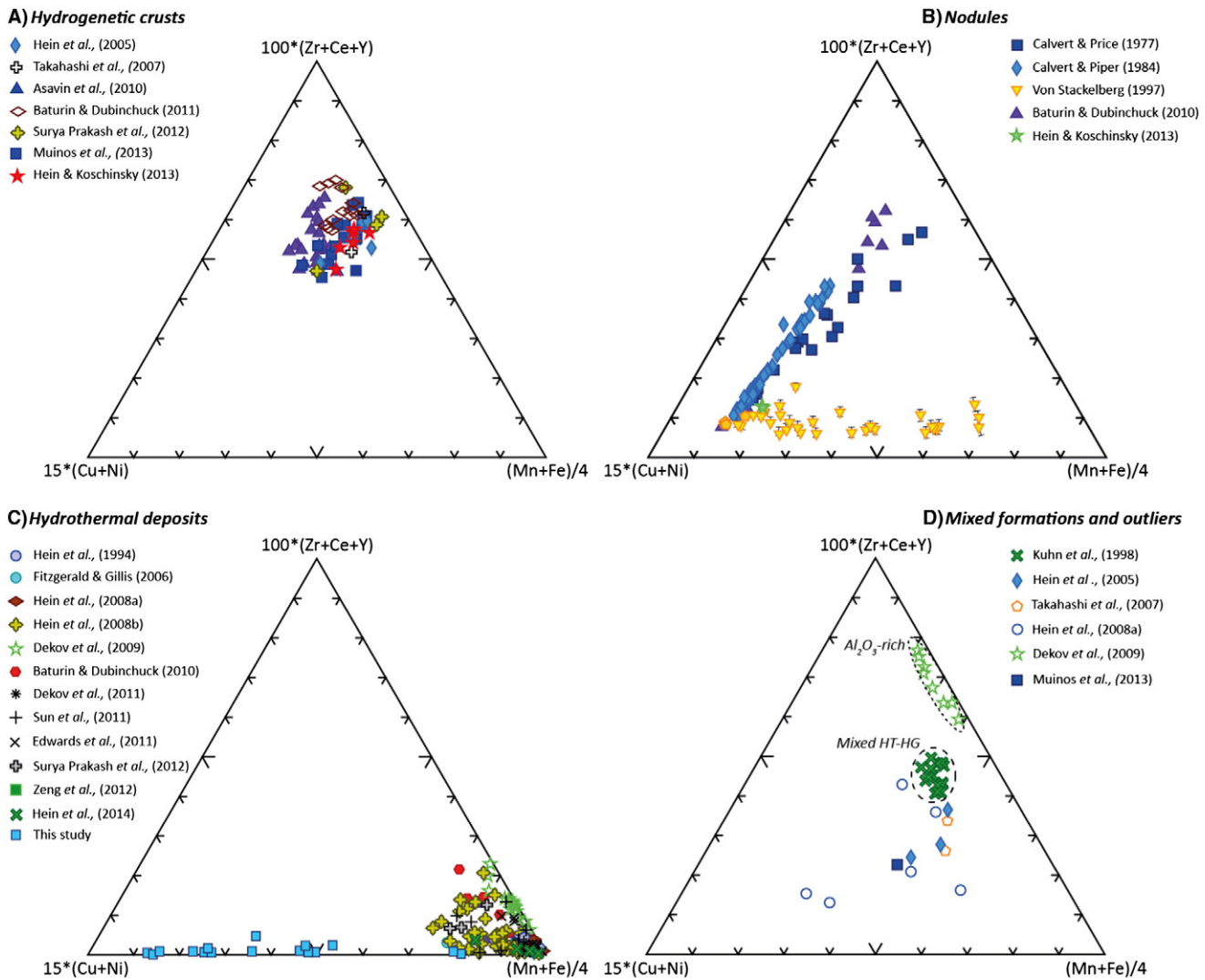


**Fig. 6.** Alternative discriminative diagram for oceanic Fe-Mn deposits using high field strength and rare earth elements. A. Hydrogenetic crusts, B. polymetallic nodules, C. hydrothermal deposits, D. mixed deposits and outliers.

a partitioning of nodule data (Fig. 6B) in accord with the position of hydrogenetic crust data. The transition from hydrogenetic to diagenetic favors high concentration in Ni and Cu at the expense of HFSE and REY defining a trend from the potential economic-metal apex with diagenetic nodules towards the REY-HFSE apex with mixed hydrogenetic-diagenetic samples. Data for diagenetic suboxic samples from the Peru Basin (Von Stackelberg, 1997) lack Y concentrations. Concentrations included in the calculation of the HFSE apex therefore used the average Y concentration of 69 ppm for Peru Basin samples from Hein and Koschinsky (2013) including a standard deviation of  $\pm 30$  ppm calculated from the nodule dataset used in this study ( $n = 184$ ). These samples define here a line moving towards the Fe-Mn apex with a consistent HFSE-REY index at the expense of the metal content. This specific nodule trend is consistent with the evolution of the bulk Ni + Cu content in polymetallic nodules described by Halbach et al. (1981). Indeed, transition from hydrogenetic to oxic diagenetic nodules favors metal enrichment with high grades of Ni + Cu with Mn/Fe ratios as high as 5. However, transition to suboxic diagenetic samples from the Peru Basin (Von Stackelberg, 1997) with a bulk Mn/Fe ratio of up to 100 displays decreasing metal contents (Halbach et al., 1981; Dymond et al., 1984). Dominant suboxic conditions favor formation of a strong gradient of Mn and Fe in the pore waters by dissolution of Mn oxides and reduction of ferric iron in the sediment in the presence of required quantities of

organic carbon. This abundance of  $\text{Mn}^{2+}$  and  $\text{Fe}^{2+}$  therefore compete with  $\text{Cu}^{2+}$  and  $\text{Ni}^{2+}$  for incorporation in the todorokite lattice promoting the shift observed in the ternary diagram (Halbach et al., 1981; Hein and Koschinsky, 2013). Detailed analysis of nodule microlayers from the Peru Basin (Wegorzewski and Kuhn, 2014) have shown that these trends are only valid when considering bulk composition and that otherwise nodules are made of alternating layers of hydrogenetic and diagenetic composition in various proportions. In the scope of this new discrimination diagram, only bulk compositions are considered.

In Fig. 6C, the use of REY and HFSE separates the overlap of metal-rich hydrothermal samples with those of hydrogenetic or diagenetic origins as compared to other schemes. Metal-rich samples from Wallis and Futuna are spread between the Fe-Mn and Cu-Ni apex. Most hydrothermal samples fall otherwise close to the Fe-Mn apex in accordance with their typical depletion in HFSE and minor metals (Cu, Ni, Co, and Zn).

#### 4.4. Limits of the discrimination diagram

Samples which do not fit the major trends observed for the majority of the dataset are presented in Fig. 6D. Most of these samples present specific atypical characteristics or constitute mixed-type deposits and allow for the exploration of the diagram's limits as to which samples

can be correctly classified using this discrimination scheme. Mixed hydrothermal-hydrogenetic crust samples (Hein et al., 2005; Muiños et al., 2013) result from the incorporation of hydrothermally derived elements into hydrogenetic crusts either as fall-out particles or acquire a hydrothermal signature through the input of LT hydrothermal fluids. Hydrogenetic samples from the Indian Ocean Ridge display such a characteristic with a faster growth rate supported by a distal hydrothermal supply which in turn impacts the time available for HFSE and REY uptake from seawater (Kuhn et al., 1998; Takahashi et al., 2007). Samples from the Southern California Borderland present Hg-Ag enrichment, Ce positive anomalies, Co and REE concentration intermediate between hydrogenetic and hydrothermal deposits which highlight a mixed hydrothermal-hydrogenetic geochemical signature (Hein et al., 2005). As observed on Fig. 6D, these samples plot in an intermediate position between hydrogenetic crusts and hydrothermal deposits, supporting the use of HFSE and REY as a discriminant in this diagram.

Some hydrothermal samples from the silica-hematite deposits (Hein et al., 2008a) display a nearly pure Silica composition with <3% Fe. These samples are scattered in the middle of the diagram due to the lack of representability of each apex considering silica dilution. Samples with Si > 70% and at least 6% Fe plot well within the hydrothermal field (Fig. 6C). It is possible to consider an apex  $(\text{Fe} + \text{Mn} + \text{Si}) / 5$  as a substitute to better accommodate specific samples with extreme Si enrichment, usually of hydrothermal origin (Supplementary Fig. S1). Comparable mineralogical impact is observed for a hydrogenetic crust sample (Muiños et al., 2013) where  $\delta\text{-MnO}_2$  is 71% and todorokite is present, compared to 85–99%  $\delta\text{-MnO}_2$  for the rest of the sample set from this area; todorokite is uncommon for open-ocean hydrogenetic crusts but common in continental margin hydrogenetic crusts (Conrad et al., 2017) which might account for the unusual signature of this sample. With regard to other samples from Muiños et al. (2013), the important presence of non Fe-Mn phases (30% of calcite and dolomite) shift the sample position towards the Fe-Mn apex.

Some hydrothermal sediments from Eolo Seamount scatter along the Fe-Mn-HFSE-REY side of the diagram far from other hydrothermal samples. This distribution highlights a strong enrichment in HFSE that is attributed to the remobilization and redeposition of hydrothermal particle mixing with detrital material (>65% clays in bulk sample) (Dekov et al., 2009).

Another limit of this diagram lies in the distinction between metal-rich hydrothermal deposits and suboxic diagenetic nodules that cover similar fields. However, although these two deposit types might plot in a similar area on the diagram, they can be distinguished by mineralogy or by plotting the Mn/Fe ratio vs  $(\text{Zr} + \text{Y} + \text{Ce})$ . Besides, these two sample types would have been collected from quite different environments and have very different appearances.

The use of this diagram as a genetic discriminant therefore requires that samples plotted in it contain >5% Fe and Mn when the major phase is silica like in the case of the silica-hematite deposits. Silica dilution of the Fe-Mn fraction can be significant (up to 95%) without changing much the appropriate positioning of samples because silica is not known to be associated with more than trace amounts of metals, HFSE and REY. If non Fe-Mn oxide minerals are present, then a >70% Fe-Mn portion is necessary to correctly discriminate sample genesis; for example with >30% carbonate, clays or sulphides, samples cannot be correctly discriminated on this diagram. Titanium and Zr must be used with caution because these elements are abundant in both volcanic rocks hosting most Fe-Mn deposits and in detrital clay minerals that may be incorporated in Fe-Mn deposits. It is therefore recommended to look for potential contamination by mafic volcanic grains from the substratum by looking for high  $\text{Al}_2\text{O}_3$  contents in bulk samples and determine, when possible, the carbonate- and clay-free fraction of metalliferous sediments to avoid the contamination by non-metalliferous material as exemplified by samples from the Eolo Seamount (Dekov et al., 2009).

#### 4.5. New discrimination diagram for Fe-Mn oceanic deposits

The data distribution in Fig. 6 supports the efficacy of HFSE and REY as a discriminant for Fe-Mn oceanic deposits, as introduced by Bau et al. (2014). As highlighted here, previously proposed discrimination schemes do not completely distinguish metal-rich hydrothermal samples from the two other dominant types of Fe-Mn deposits, as well as separation of mixed deposit types. In addition, phosphatized hydrogenetic crust samples are positioned within this diagram among other crusts. Consequently this new scheme provides increased sensitivity for discrimination among the genetic processes that produced these various deposit types, and thus provides a powerful tool.

Based on data distribution on this ternary diagram, we propose the following identification of genetic fields for the formation of oceanic Fe-Mn deposits (Fig. 7). This figure displays the detailed relations among the three genetic processes through well-defined fields for each deposit-forming process without overlap of metal-rich hydrothermal samples and hydrogenetic samples. This scheme allows for the identification of fields possibly representative of oxic and suboxic diagenesis within nodules, the trend between hydrogenetic and diagenetic end-members that forms a continuum, and identifies mixed genetic types such as the presence of hydrothermal particles within hydrogenetic crusts. This scheme does group hydrothermal Fe oxides and Mn oxides into a single field.

#### 4.6. Alternative classifications for driving exploration at sea

Although robust, the new discrimination scheme (this study) and the discrimination diagrams proposed by Bau et al. (2014) cannot be easily applied to historical data because of the lack of REE and HFSE data. Additionally, analyses of REE requires land-based analytical techniques and thus discrimination of Fe-Mn mineralization using REE cannot be done at sea, which would help direct exploration. As a consequence, we investigated alternatives to the  $100 * (\text{Zr} + \text{Ce} + \text{Y})$  apex using elements that are widely available in the literature (e.g. Ti, Co and Ce) and/or that can be analyzed at sea using a compact, benchtop ED-XRF spectrometer (e.g. Ti, Co, Zr and Y). The ship-board proposed apexes for ternary diagrams include: (A)  $20 * \text{Ti}$ , (B)  $50 * \text{Co}$ , (C)  $50 * \text{Ce}$ , (D)  $30 * (\text{Co} + \text{Ce})$ , (E)  $50 * (\text{Ti}/5 + \text{Ce})$ , and (F)  $200 * (\text{Zr} + \text{Y})$  (Supplementary Fig. S2), with all elements expressed in wt.%.

A Ti apex brings a lot of uncertainty and scattering, notably for hydrothermal samples, probably due to contamination of samples by the protolith, which increases the HFSE elements. The presence of the protolith within the mineralized sample is relatively common during sampling and its influence can be verified in this configuration by checking the amount of aluminum. Compared with the hydrothermal field identified in Fig. 7, samples spreading towards the HFSE apex exhibit increasing Al content mostly above 2% and up to 7.7% whereas samples correctly positioned have <0.9% Al.

Combinations using Co works well as a discriminant for most Fe-Mn deposits but fail to accommodate Co-rich hydrothermal deposits such as samples from Wallis and Futuna. The use of only Ce as an apex also works in the absence of Zr and Y data, however it therefore represents incorporation dominantly through Mn oxides. In addition, discrimination between hydrothermal samples and diagenetic nodules cannot be made solely on the basis of this diagram owing to their similar contents of Ce. As exemplified in previous combinations, Ce constitutes the most effective discriminant among the REE and HFSE for deep-sea Fe-Mn deposits. It can therefore be used as a viable apex in the absence of more complete data, although it is not adapted for on-board exploration as instrumental errors are important for Ce measurement by ED-XRF. Consequently, the scheme which uses the  $200 * (\text{Zr} + \text{Y})$  apex represents the best alternative to our preferred discrimination diagram to use at sea. In the absence of data for Ce, the zone for the hydrogenetic crust is less restrictive but interestingly, Zr and Y can be easily determined at sea using

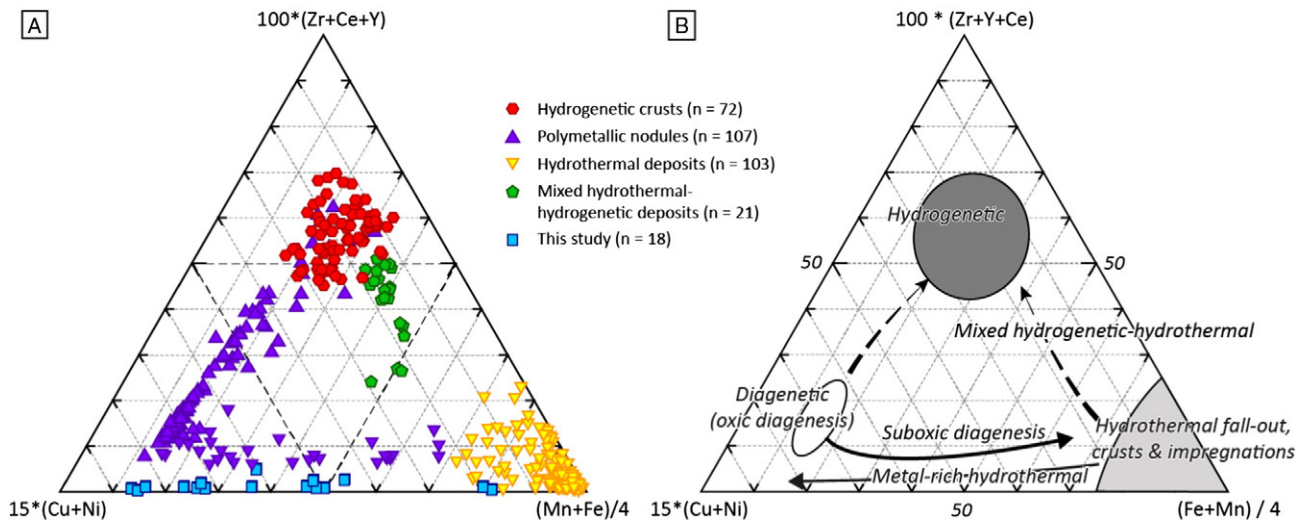


**Fig. 7.** (A) Ternary discriminative diagram for genetic classification of oceanic ferromanganese deposits displaying all samples used in this study and (B) corresponding genetic fields. The dashed arrows present the mixing trends between two genetic processes highlighting the continuum between hydrogenetic-hydrothermal crusts and hydrogenetic-diagenetic nodules. Solid arrows show trends of a sample set related to only one genetic process.

a compact, benchtop ED-XRF spectrometer (Fig. S3; supplementary information). This easy-to-use discrimination diagram, aside from deciphering the nature of Fe-Mn  $\pm$  Si mineralization (i.e. hydrogenetic crusts, polymetallic nodules and metal-rich/metal-poor hydrothermal precipitates), would be useful for driving deep-sea exploration campaigns.

## 5. Conclusions

Oceanic Fe-Mn deposits have major differences in HFSE enrichments and REE signatures. Such features can be used and incorporated into a new discrimination scheme. Hydrogenetic crusts possess high HFSE concentrations with strong positive Ce anomaly, followed closely by concentrations in polymetallic nodules, whereas hydrothermal Fe-Mn precipitates show relative depletion in HFSE, with a negative Ce anomaly. The relation between deposit-forming processes and Fe, Mn, Cu, Ni, Co, HFSE and REY concentrations has also been demonstrated for each type of Fe-Mn deposit. Trace element enrichments such as Co, Zr, Ti and REY are favored by hydrogenetic precipitation, whereas diagenetic processes provide higher Mn, Cu, and Ni concentrations when diagenetic remobilization occurs in the sediment column. Hydrothermal Fe-Mn deposits show strong depletion in Zr, Ti and REY due to rapid formation and strongly variable metal contents of fluids. Taking these differences into account, a ternary diagram was developed that clearly discriminates the various Fe-Mn deposit types. The ternary diagram uses metals – HFSE–Fe-Mn that distinguish the main deposit-forming processes and the interaction of those processes that form mixed-type diagenetic-hydrogenetic nodules and hydrogenetic-hydrothermal crusts, as well as possibly distinguishing oxic-suboxic bulk diagenetic deposits, and variable metal enrichment in hydrothermal deposits. Finally, we propose an easy-to-use version of this diagram to discriminate seafloor Fe-Mn precipitates that can be used on-board ships for driving deep-sea exploration projects using XRF measurements.

## Acknowledgement

We thank the crews of R/V l'Atalante and Nautille HOV (Ifremer, France) and all participants of the FUTUNA cruise (chief scientist: Y. Fouquet) for their assistance at sea. The authors would like to thank G. Bayon for his help on the method used for ICP measurements, A.S. Alix for the GIS data management and P. Fernagu for the preparation of

polished sections. The authors would like to thank ERAMET, AREVA, TECHNIP, BRGM, and AMP for their financial support for the FUTUNA (2010) cruise. We are thankful as well for the review and helpful discussion with J.R. Hein and an anonymous reviewer.

## Appendix A. Supplementary data

Supplementary data to this article can be found online at <http://dx.doi.org/10.1016/j.oregeorev.2016.09.003>.

## References

- Alt, J.C., 1988. Hydrothermal oxide and nontronite deposits on seamounts in the eastern Pacific. *Mar. Geol.* 81, 227–239.
- Aplin, A.C., Cronan, D.S., 1985. Ferromanganese oxide deposits from the central Pacific Ocean, II. Nodules and associated sediments. *Geochim. Cosmochim. Acta* 49, 437–451.
- Asavin, A.M., Kubrakova, I.V., Mel'nikov, M.E., Tyutyunnik, O.A., Chesalova, E.I., 2010. Geochemical zoning in ferromanganese crusts of Ita-MaiTai guyot. *Geochem. Int.* 48, 423–445.
- Balaran, V., Anjaiah, K.V., Reddy, M.R.P., 1995. Comparative study on the trace and rare earth element analysis of an Indian polymetallic nodule reference sample by inductively coupled plasma atomic emission spectrometry and inductively coupled plasma mass spectrometry. *Analyst* 120, 1401–1406.
- Barrat, J.A., Keller, F., Amosse, J., Taylor, R.N., Nesbitt, R.W., Hirata, T., 1996. Determination of rare earth elements in sixteen silicate reference samples by ICP-MS after Tm addition and ion exchange separation. *Geostand. Newslett.* 20, 133–139.
- Barret, T.J., Jarvis, I., 1988. Rare earth element geochemistry of metalliferous sediments from DSDP Leg 92: the East Pacific Rise Transect. *Chem. Geol.* 67, 243–259.
- Barret, T.J., Taylor, P.N., Lugooski, J., 1987. Metalliferous sediments from DSDP Leg 92: the East Pacific Rise Transect. *Geochim. Cosmochim. Acta* 51, 2241–2253.
- Baturin, G.N., Dubinchuk, V.T., 2009. Composition of ferromanganese nodules from Riga Bay (Baltic Sea). *Oceanology* 49, 111–120.
- Baturin, G.N., Dubinchuk, V.T., 2010. On the composition of ferromanganese nodules of the Indian Ocean. *Dokl. Earth Sci.* 434, 1179–1183.
- Baturin, G.N., Dubinchuk, V.T., 2011. Mineralogy and chemistry of ferromanganese crusts from the Atlantic Ocean. *Geochem. Int.* 48, 578–593.
- Baturin, G.N., Dubinchuk, V.T., Rashidov, V.A., 2010. Composition of Fe-Mn Crusts from Okhotsk Sea. *Minerals of the Ocean-5 & Deep-sea Minerals and Mining-2 Joint International Conference. St. Petersburg, Russia, 28th June–1st July*, p. 2010.
- Bau, M., 1991. Rare-earth element mobility during hydrothermal and metamorphic fluid-rock interaction and the significance of the oxidation state of europium. *Chem. Geol.* 93, 219–230.
- Bau, M., Koschinsky, A., 2009. Oxidative scavenging of cerium on hydrous Fe oxide: evidence from the distribution of rare earth elements and yttrium between Fe oxides and Mn oxides in hydrogenetic ferromanganese crusts. *Geochim. J.* 43, 37–47.
- Bau, M., Koschinsky, A., Dulski, P., Hein, J.R., 1996. Comparison of the partitioning behaviours of yttrium, rare earth elements, and titanium between hydrogenetic marine ferromanganese crusts and seawater. *Geochim. Cosmochim. Acta* 60, 1709–1725.



- Bau, M., Schmidt, K., Koschinsky, A., Hein, J.R., Usui, A., 2014. Discriminating between different genetic types of marine ferro-manganese crusts and nodules based on rare earth elements and yttrium. *Chem. Geol.* 381, 1–9.
- Bonatti, E., 1975. Metallogenesis at oceanic spreading centers. *Annu. Rev. Earth Planet. Sci.* 3, 401–431.
- Bonatti, E., Kraemer, T., Rydell, H., 1972. Classification and genesis of submarine iron-manganese deposits. In: HORN, D. (Ed.), *Ferromanganese Deposits on the Ocean Floor*. Natl. Sci. Found., Washington, pp. 149–165.
- Bruland, K.W., 1983. Trace elements in seawater. In: RIPLEY, J.P., CHESTER, R. (Eds.), *Chemical Oceanography*. Academic Press, pp. 157–200 (1983).
- Burgath, K.P., Von Stackelberg, U., 1995. Sulfide-impregnated volcanics and ferromanganese incrustations from the southern Lau Basin (southwest Pacific). *Mar. Georesour. Geotechnol.* 13, 263–308.
- Calvert, S.E., Piper, D.Z., 1984. Geochemistry of ferromanganese nodules from DOMES Site A, northern equatorial Pacific: multiple diagenetic metal source in the deep sea. *Geochim. Cosmochim. Acta* 48, 1913–1928.
- Calvert, S.E., Price, N.B., 1977. Geochemical variation in ferromanganese nodules and associated sediments from the Pacific Ocean. *Mar. Chem.* 5, 43–74.
- Cann, J.R., Winter, C.K., Pritchard, R.G., 1977. A hydrothermal deposit from the floor of the Gulf of Aden. *Mineral. Mag. Lond.* 41, 193–199.
- Choi, J.H., Hariya, Y., 1992. Geochemistry and depositional environment of Mn oxide deposits in the Tokoro Belt, northeastern Hokkaido, Japan. *Econ. Geol.* 87, 1265–1274.
- Conly, A.G., Scott, S.D., Bellon, H., 2011. Metalliferous manganese oxide mineralization associated with the Boléo Cu-Co-Zn district, Mexico. *Econ. Geol.* 106, 1173–1196.
- Conrad, T., Hein, J.R., Paytan, A., Clague, D.A., 2017. Formation of Fe-Mn crusts within a continental margin environment. *Ore Geol. Rev.* 87, 25–40.
- Corliss, J.B., Lyle, M., Dymond, J., Crane, K., 1978. The chemistry of hydrothermal mounds near the Galapagos rift. *Earth Planet. Sci. Lett.* 40, 12–24.
- Craddock, P.R., Bach, W., Seewald, J.S., Rouxel, O.J., Reeves, E., Tivet, M.K., 2010. Rare earth element abundances in hydrothermal fluids from the Manus Basin, Papua New Guinea: indicators of sub-seafloor hydrothermal processes in back-arc basins. *Geochim. Cosmochim. Acta* 74, 5494–5513.
- De Carlo, E.H., Mc Murtry, G.M., 1992. Rare-earth element geochemistry of ferromanganese crusts from the Hawaiian Archipelago, central Pacific. *Chem. Geol.* 95, 235–250.
- Dekov, V.M., Kamenov, G.D., Savelli, C., Stummeyer, J., Thiry, M., Shanks, W.C., Willingham, A.L., Boycheva, T.B., Rochette, P., Kuzmann, E., Fortin, D., Vértés, A., 2009. Metalliferous sediments from Eolo Seamount (Tyrrhenian Sea): hydrothermal deposition and re-deposition in a zone of oxygen depletion. *Chem. Geol.* 264, 347–363.
- Dekov, V.M., Boycheva, T.B., Halenius, U., Billstrom, K., Kamenov, G.D., Shanks, W.C., Stummeyer, J., 2011. Mineralogical and geochemical evidence for hydrothermal activity at the west wall of 12°50'N core complex (Mid-Atlantic ridge): a new ultramafic-hosted seafloor hydrothermal deposit? *H. S. and R – control of mineralogical and chemical composition by multiple accretionary processes*. *Geochim. Cosmochim. Acta* 48, 931–949.
- Edmonds, H.N., German, C.R., 2004. Particle geochemistry in the Rainbow hydrothermal plume, Mid-Atlantic Ridge. *Geochim. Cosmochim. Acta* 68, 759–772.
- Edwards, K.J., Glazer, B.T., Rouxel, O.J., Bach, W., Emerson, D., Davis, R.E., Toner, B.M., Chan, C.S., Tebo, B.M., Staudigel, H., Moyer, C.L., 2011. Ultra-diffuse hydrothermal venting supports Fe-oxidizing bacteria and massive umber deposition at 5000 m off Hawaii. *Int. Soc. Microb. Ecol.* 5, 1748–1758.
- Fitzgerald, C.E., Gillis, K.M., 2006. Hydrothermal manganese oxide deposits from Baby Bare seamount in the Northeast Pacific Ocean. *Mar. Geol.* 225, 145–156.
- Fouquet, Y., Von Stackelberg, U., Charlou, J.L., Erzinger, J., Herzig, P.M., Muehe, R., Wiedicke, M., 1993. Metallogenesis in back-arc environments: the Lau Basin example. *Econ. Geol.* 88, 2154–2181.
- Fouquet, Y., Scalabrin, C., Alix, A.S., Donval, J.P., Dupré, S., Guérin, C., Guillou, M., Guyader, V., Konn, C., Patriat, M., Pelletier, E., Pierre, D., Rosazza, F., Saint-Laurent, X., Dymont, J., Szticar, F., 2015. Multi scales exploration strategy – example of research for hydrothermal mineralization in the French EEZ of Wallis and Futuna. *Offshore Technology Conference*, 04–07 May, Houston, Texas, USA.
- German, C.R., Colley, S., Palmer, M.R., Khripounoff, A., Klinkhammer, G.P., 2002. Hydrothermal plume-particle fluxes at 13°N on the East Pacific Rise. *Deep-Sea Res. I Oceanogr. Res. Pap.* 49, 1921–1940.
- Goulding, H.C., Mills, R.A., Nesbitt, R.W., 1998. Precipitation of hydrothermal sediments on the active TAG mound: implications for ochre formation. In: Mills, R.A., Harrison, K. (Eds.), *Modern Ocean Floor Processes and the Geological Record*. Geological Society, London, Special Publications 148, pp. 201–216.
- Halbach, P., Puteanus, D., 1988. Geochemical trends of different genetic types of nodules and crusts. In: Halbach, P., Friedrich, G., Von Stackelberg, U. (Eds.), *The Manganese Nodule Belt of the Pacific Ocean*. Ferdinand Enke, Stuttgart, pp. 61–69 ((1988) Chapter 4).
- Halbach, P., Scherhag, C., Hebisch, U., Marchig, V., 1981. Geochemical and mineralogical control of different genetic types of deep-sea nodules from the Pacific Ocean. *Mineral. Deposita* 16, 59–84.
- Halbach, P., Friedrich, G., Von Stackelberg, U., 1988. *The Manganese Nodule Belt of the Pacific Ocean Geological Environment, Nodule Formation, and Mining Aspects*. Enke Verlag, Stuttgart ((1988) 245 pp.).
- Hein, J.R., Koschinsky, A., 2013. Deep-ocean ferromanganese crusts and nodules. In: Holland, H.D., Turekian, K.K. (Eds.), 2nd Ed. *Treatise on Geochemistry* vol. 13. Elsevier, Amsterdam, pp. 273–291 (Chapter 11).
- Hein, J.R., Yeh, H.-W., Gunn, S.H., Gibbs, A.E., Wang, C.-H., 1994. Composition and origin of hydrothermal ironstones from central Pacific seamounts. *Geochim. Cosmochim. Acta* 58, 179–189.
- Hein, J.R., Gibbs, A.E., Clague, D.A., Torresan, M., 1996. Hydrothermal mineralization along submarine rift zones, Hawaii. *Mar. Georesour. Geotechnol.* 14, 177–203.
- Hein, J.R., Koschinsky, A., Halbach, P., Manheim, F.T., Bau, M., Kang, J.-K., Lubik, N., 1997. Iron and manganese oxide mineralization in the Pacific. In: Nicholson, K., Hein, J.R., Bühn, B., Dasgupta, S. (Eds.), *Manganese Mineralization: Geochemistry and Mineralogy of Terrestrial and Marine Deposits*, pp. 123–138.
- Hein, J.R., Koschinsky, A., Bau, M., Manheim, F.T., Kang, J.-K., Roberts, L., 2000. Cobalt-rich ferromanganese crusts in the Pacific. In: Cronan, D.S. (Ed.), *Handbook of Marine Minerals Deposit*. CRC Press, Boca Raton, Florida, pp. 239–279.
- Hein, J.R., Koschinsky, A., McIntyre, B.R., 2005. Mercury- and silver-rich ferromanganese oxides, southern California borderland: deposit model and environmental implications. *Econ. Geol.* 100, 1151–1168.
- Hein, J.R., Clague, D.A., Koski, R.A., Embley, R.W., Dunham, R.E., 2008a. Metalliferous sediment and a silica-hematite deposit within the Blanco Fracture Zone, northeast Pacific. *Mar. Georesour. Geotechnol.* 26 (4), 317–339.
- Hein, J.R., Schulz, M.S., Dunham, R.E., Stern, R.J., Bloomer, S.H., 2008b. Diffuse flow hydrothermal manganese mineralization along the active Mariana and southern Izu-Bonin arc system, western Pacific. *J. Geophys. Res.* 113 (B08S14, 29pp.).
- Hein, J.R., Mizell, K., Koschinsky, A., Conrad, T.A., 2013. Deep-ocean mineral deposits as a source of critical metals for high- and green-technology applications: comparison with land-based resources. *Ore Geol. Rev.* 51, 1–14.
- Hein, J.R., Ronde, C.E.J., Koski, R.A., Ditchburn, R.G., Mizell, K., Tamura, Y., Stern, R.J., Conrad, T.A., Ishizuka, O., Leybourne, M.J., 2014. Layered hydrothermal barite-sulfide mound field, East Diamante caldera, Mariana volcanic arc. *Econ. Geol.* 109, 2179–2206.
- Jung, H.-S., Lee, C.-B., 1999. Growth of diagenetic ferromanganese nodules in an oxic deep-sea sedimentary environment, northeast equatorial Pacific. *Mar. Geol.* 157, 127–144.
- Koschinsky, A., Fritsche, U., Winkler, A., 2001. Sequential leaching of Peru Basin surface sediment for the assessment of aged and fresh heavy metal associations and mobility. *Deep-Sea Res. II Top. Stud. Oceanogr.* 48, 3683–3699.
- Kuhn, T., Bau, M., Blum, N., Halbach, P., 1998. Origin of negative Ce anomalies in mixed hydrothermal-hydrogenetic Fe-Mn crusts from the Central Indian Ridge. *Earth Planet. Sci. Lett.* 163, 207–220.
- Kuhn, T., Bostick, B.C., Koschinsky, A., Halbach, P., Fendorf, S., 2003. Enrichment of Mo in hydrothermal Mn precipitates: possible Mo sources, formation process and phase associations. *Chem. Geol.* 199, 29–43.
- Michard, A., 1989. Rare earth element systematics in hydrothermal fluids. *Geochim. Cosmochim. Acta* 53, 745–750.
- Mills, R.A., Wells, D.M., Roberts, S., 2001. Genesis of ferromanganese crusts from the TAG hydrothermal field. *Chem. Geol.* 176, 283–293.
- Muñoz, S.B., Hein, J.R., Frank, M., Monteiro, J.H., Gaspar, L., Conrad, T., Pereira, G., Abrantes, F., 2013. Deep-sea Fe-Mn crusts from the northeast Atlantic Ocean: composition and resource considerations. *Mar. Georesour. Geotechnol.* 31, 40–70.
- Nicholson, K., 1992. Contrasting mineralogical-geochemical signatures of manganese oxides: guides to metallogenesis. *Econ. Geol.* 87, 1253–1264.
- Ohta, A., Ishii, S., Sakakibara, M., Mizuno, A., Kawabe, I., 1999. Systematic correlation of the Ce anomaly with the Co/(Ni + Cu) ratio and Y fractionation from Ho in distinct types of Pacific deep-sea nodules. *Geochim. J.* 33, 399–417.
- Pattan, J.N., Banakar, V.K., 1993. Rare earth element distribution and behaviour in buried manganese nodules from the Central India Basin. *Mar. Geol.* 112, 303–312.
- Pelletier, E., Fouquet, Y., Etoubleau, J., Cheron, S., Labanieh, S., Josso, P., Langlade, J., 2017. Ni-Cu-Co-rich hydrothermal manganese mineralization in the Wallis and Futuna back-arc environment (SW Pacific). *Ore Geol. Rev.* 87, 126–146.
- Pelletier, B., Lagabrielle, Y., Benoit, M., Cabioch, G., Calmant, S., Garel, E., Guivel, C., 2001. Newly identified segments of the Pacific-Australia plate boundary along the North Fiji transform zone. *Earth Planet. Sci. Lett.* 193, 347–358.
- Pourret, O., Davranche, M., 2013. Rare earth element sorption onto hydrous manganese oxide: a modeling study. *J. Colloid Interface Sci.* 395, 18–23.
- Schiff, J., Christenson, E.A., Byrne, R.H., 2015. YREE scavenging in seawater: a new look at an old model. *Mar. Chem.* 177 (Part 3), 460–471.
- Schmidt, K., Bau, M., Hein, J., Koschinsky, A., 2014. Fractionation of the geochemical twins Zr-Hf and Nb-Ta during scavenging from seawater by hydrogenetic ferromanganese crusts. *Geochim. Cosmochim. Acta*.
- Schultz, H.D., 2006. Quantification of early diagenesis: dissolved constituents in pore water and signals in the solid phase. In: Schultz, H.D., Zabel, M. (Eds.), *Marine Geochemistry*, 2nd ed. Springer, Heidelberg, pp. 75–77.
- Severmann, S., Mills, R.A., Palmer, M.R., Fallick, A.E., 2004. The origin of clay minerals in active and relict hydrothermal deposits. *Geochim. Cosmochim. Acta* 68, 73–88.
- Sun, Z., Zhou, H., Yang, Q., Sun, Z., Bao, S., Yao, H., 2011. Hydrothermal Fe-Si-Mn oxide deposits from the central and south Valu Fa Ridge, Lau Basin. *Appl. Geochem.* 26, 1192–1204.
- Sun, Z., Zhou, H., Glasby, G.P., Yang, Q., Yin, X., Li, J., Chen, Z., 2012. Formation of Fe-Mn-Si oxide and nontronite deposits in hydrothermal fields on the Valu Fa Ridge, Lau Basin. *J. Asian Earth Sci.* 43, 64–76.
- Surya Prakash, L., Ray, D., Paropkari, A.L., Mudholkar, A.V., Satyanarayanan, M., Sreenivas, B., Chandrasekharan, D., Kota, D., Kamesh Raju, K.A., Kaisary, S., Balaram, V., Gurav, T., 2012. Distribution of REEs and yttrium among major geochemical phases of marine

- Fe–Mn-oxides: comparative study between hydrogenous and hydrothermal deposits. *Chem. Geol.* 312–313, 127–137.
- Takahashi, Y., Manceau, A., Geoffroy, N., Marcus, M.A., Usui, A., 2007. Chemical and structural control of the partitioning of Co, Ce, and Pb in marine ferromanganese oxides. *Geochim. Cosmochim. Acta* 71, 984–1008.
- Taylor, S.R., McLennan, S.M., 1985. *The Continental Crust: Its Composition and Evolution*. Blackwell Scientific, Boston, Mass (312 pp.).
- Von Stackelberg, U., 1997. Growth history of manganese nodules and crusts of the Peru Basin. In: Nicholson, K., Hein, J.R., Bühn, B., Dasgupta, S. (Eds.), *Manganese Mineralization: Geochemistry and Mineralogy of Terrestrial and Marine Deposits*, pp. 153–176.
- Wegorzewski, A.V., Kuhn, T., 2014. The influence of suboxic diagenesis on the formation of manganese nodules in the Clarion Clipperton nodule belt of the Pacific Ocean. *Mar. Geol.*
- Zeng, Z., Ouyang, H., Yin, X., Chen, S., Wang, X., Wu, L., 2012. Formation of Fe–Si–Mn oxyhydroxides at the PACMANUS hydrothermal field, eastern Manus Basin: mineralogical and geochemical evidence. *J. Asian Earth Sci.* 60, 130–146.